



## Simulation of airborne collision between a drone and an aircraft nose

Xiaohua Lu <sup>a,\*</sup>, Xinchao Liu <sup>b,\*</sup>, Yingchun Zhang <sup>c</sup>, Yulong Li <sup>d</sup>, Hongfu Zuo <sup>a</sup>



<sup>a</sup> College of Civil Aviation, Nanjing University of Aeronautics and Astronautics, Nanjing, China  
<sup>b</sup> Department of Industrial Engineering, University of Arkansas, Fayetteville, United States of America  
<sup>c</sup> Shanghai Aircraft Airworthiness Certification Center, Shanghai, China  
<sup>d</sup> Aeronautics College, Northwestern Polytechnical University, Xi'an, China

### ARTICLE INFO

#### Article history:

Received 10 February 2020  
 Received in revised form 19 August 2021  
 Accepted 23 August 2021  
 Available online 30 August 2021  
 Communicated by Jang-Kyo Kim

#### Keywords:

Collision simulation  
 Test validation  
 UAV  
 Aircraft nose  
 Safety evaluation  
 Airworthiness

### ABSTRACT

The usage of a large number of civil unmanned aerial vehicles (UAVs) has caused potential hazards to the safe operation of manned aircraft. In this paper, a full-size commercial aircraft nose and a typical UAV with the whole level were selected for collision test, by which the verified finite element (FE) models were applied to four representative regions of the nose for collision simulation. A 1,360 g UAV and a 1,800 g bird have collided with the nose respectively under the same conditions and the former caused more serious damage. The kinetic energy of UAV as well as the hardness of its major components plays a critical role in evaluating damage of the nose, and the greater the kinetic energy loss, the more serious the damage of the nose is in general. It was very possible that the battery of UAV would penetrate the skin to enter the inside of nose with high speed and cause explosion and fire. The flying posture of UAV has an effect on the nose damage and no penetration happened to the lower panel of the main windshield under various possible impact postures of UAV with a velocity of 152 m/s. The existing anti-bird strike airworthiness clauses concerning the aircraft nose as CCAR 25.571 are not suitable for the design of nose against UAV strike and are suggested to be improved with extensive research findings in the future, including the operational requirements of UAVs and the design guidelines for a UAV collision mitigation.

© 2021 Elsevier Masson SAS. All rights reserved.

## 1. Introduction

With the cumulative maturity of relevant unmanned aerial vehicle (UAV) technologies and the increasing demand for UAV systems, civilian UAVs have been widely applied to various fields around the world, such as emergency rescue, environmental monitoring, electric line patrol, aerial surveying and mapping, agricultural, forestry and plant protection, as well as cargo transportation. The surge of UAVs entailed the occurrence of potential dangers and aviation accidents. In the events documented by the US, Canada, the UK, Mozambique, China, etc, UAVs directly collided with aircraft or illegally invaded into air routes. Such "black-flight" and "navigation-disturbance" incidents have resulted in the adjustment, avoidance, alternate landing, delay and grounding of multiple scheduled flights and even caused airport closure, considerably affecting millions of travelers. These events have had a much unfriendly effect on the safe operation of the civil aviation transportation industry and provoked widespread public concerns regarding aviation safety. The unknown collision consequences are

the reasons why airlines are cautious and fearful when an aircraft is approaching to UAVs. Commercial airplanes have been required to fulfill the bird-strike resistance airworthiness clauses at the design stage, whereas systematic research has not been conducted globally on the collision consequences between transportation airplanes and UAVs. Moreover, relevant airworthiness clauses that can test the safety of planes for collisions with UAVs do not yet exist.

A few civil aviation authorities of developed countries have already conducted relevant investigations. For instance, the Federal Aviation Administration (FAA) has completed a series of studies on the severity evaluation of ground collision and airborne collision of light UAVs. Moreover, it has formulated Part 107 of the Federal Aviation Regulations (FAR) based upon the conclusions of the severity evaluation regarding ground collision [1]. In the severity evaluation research on airborne collision, the Alliance for System Safety of UAS through Research Excellence (ASSURE) group (led by the FAA) has conducted certain numerical simulations, in which a quadcopter UAV and a fixed-wing UAV collided with two types of aircraft windshield, wing leading edge, tailfin leading edge and the high-speed rotating blades of an aero-engine [2–5]. Furthermore, based on the empirical penetration formula, the Australia Civil Aviation Safety Authority (ACASA) estimated the critical pen-

\* Corresponding authors.

E-mail addresses: [luxiaohua@nuaa.edu.cn](mailto:luxiaohua@nuaa.edu.cn) (X. Lu), [xi037@uark.edu](mailto:xi037@uark.edu) (X. Liu).

etration speed value of key parts of a UAV, including the camera, motor, and battery, upon penetrating the skin and windshield of a manned aircraft [6]. Institutions such as the British Transport Department have conducted numerical simulations and tests on a small-size UAV quadcopter that collided with a helicopter, the windshield of an airliner, and an airliner structure. However, limited by the caliber of the air cannon, the arms of the UAV were disassembled during the test, thereby altering the actual construction of the UAV [7]. X. Lu et al. [8] studied the collision between whole-level drones and a full-scale aircraft windshield and analyzed the damage influence factors and safety consequences. Meng X. et al. [9] performed a collision simulation between a structure-level UAS and a horizontal-stabilizer section of a commercial airliner to investigate the dynamic response of primary-operation components using the PAM-CRASH algorithm and the results revealed that a 3,400 g drone impact on an aircraft that traveled at cruising speed could penetrate the leading-edge skins on the horizontal stabilizer, which is more austere than a 3,600 g bird strike. Chen C. et al. [10] studied the dropping test and numerical simulation for unmanned aerial vehicles and the impact load and damage of UAV at different speeds, heading angles and pitch angles were simulated and analyzed. Apart from the collision between UAV and skin or windshield of manned aircraft, the aero-engines are also facing to huge risks of UAV ingestion, which would result in major safety hazards. In addition, Song et al. [11,12] comparatively analyzed the "absorption" of a bird and a UAV by the engine and conducted a parametric study on the strike angle and strike location of the UAV. Liu H. et al. [13,14] investigated the damage of fan blades and the percentage of thrust loss after UAV airborne collision to manned aircraft engine, in which different collision configurations, collision positions, and flight phases were considered and a few quantitative conclusions were drawn. Especially, a harmless-categorized drone with 250 g weight and a much higher weight drone with 750 g were simulated to collide with engine respectively and compared to each other [15]. Lyons T. et al. [16] carried out the simulation of the ingestion of the quadcopter UAV model into a business jet engine fan assembly model, and particular parameters studies showed that takeoff scenario resulted in the greatest damage to the fan blades mainly caused by the motor, camera, and battery of the quadcopter.

In the present paper it focuses on the scene where the typical positions of the nose are struck by UAVs. According to the CCAR25.571 of the Civil Aviation Administration of China, the damage tolerance (discrete source) of an aircraft structure needs to fulfill the following requirements. When an aircraft is struck by a bird of 1,800 g (4 lb) weight at the relative velocity at sea level, namely VC or 0.85 VC, it should be able to complete the flight successfully. Statistics have shown that the probability of the aircraft's nose structure being damaged from a bird strike accounts for 44% of the entire aircraft damage [17]. The nose structure includes critical parts, such as the windshield, canopy, side sheet, and radome. Those parts are given special attention during the design phase of bird-strike resistance and UAV collision resistance. After investigating the dynamic response of the side-sheet structure of a civil aircraft to bird strike through the PAM-CRASH platform, Qiu L. et al. [18] proposed the optimization scheme of bird-strike resistance by strengthening the stiffness of the weakest zone at the side sheet of the canopy. With the application of the PAM-CRASH platform, Wang J. et al. [19] verified the bird-strike resistance of the top structure of the civil aircraft nose and performed material-layer optimization. In addition, Liu J. et al. [20] proposed the SPH-FE coupling method to conduct a numerical simulation study and an experimental verification for the case of a bird strike on a civil aircraft side sheet by using the PAM-CRASH platform. Zhou Y. et al. [21,22] investigated bird-strike damages of composite laminates layups and circular laminated plate employing SPH and FE anal-

ysis. The results would be used to improve the anti-bird impact design of composite laminates structures through the research of energy variations, including kinetic, strain, and damage dissipations and rotational speeds. Ballistic gelatine and rubber projectiles were used to replace the real birds for experimental and simulation study of strike on the aircrafts' fuselage and windshield because of cost and replicability [23]. Currently, the crashworthiness of the key parts of a commercial aircraft' nose by UAVs remains unavailable. However, the aforementioned research findings on bird strikes on various kinds of aircraft can provide a reference for the collision between a UAV and a nose structure when the impact velocity, weight of the UAV, and impact point are considered. They can be used as a comparison for the assessment of damage extent in addition. Meanwhile, dynamic behavior analysis for UAVs and bird striking on the aircraft nose under similar conditions is addressed to verify whether the existing airworthiness regulation requirements for aircraft anti-bird impacts were suited to aircraft anti-drone impacts.

The weight of a Phantom4 UAV (approximately 1,360 g) produced by DJI-Innovations (DJI) is closest to that of a bird (1,800 g) in all of DJI products and has a broad representation in use. In the present study, the Phantom4 UAV, along with a specific model commercial aircraft nose structure, will be investigated. The mid-air collision between the UAV and the canopy, the side sheet, and the lower plate of the nose will be simulated based on a validated model of the collision test between a full-size nose and a whole-level UAV. The result under the aforementioned conditions will be compared with a bird strike. The assessment of the severity of the UAV striking on the aircraft's nose will be presented, which could provide technological support for the formulation of more trustworthy and persuasive airworthiness regulations.

## 2. Finite element (FE) simulation model

### 2.1. FE model of the aircraft nose

The entire nose structure was discretized along with the shell unit. The dimension ratio, calculation accuracy, and computational efficiency of the structural parts of the nose were comprehensively considered. The external features of the geometrical model were extracted from the source file in CATIA format, after which the details of the model were amended in the HyperMesh environment, and the pre-treatment of the calculation model was performed after importing the model into PAM-CRASH finally. All shell units were four-node integration-reduced S4R units, and nine integrations were set along with the thickness of the shell unit. Furthermore, the side length of a single unit was set as 7 mm, and the total number of units was 691,221. All rivets were set as the Plink units and the total number of units was 8,226. The FE model of the nose is presented in Fig. 1.

The mechanical behavior of the nose structural parts complied with the No. 102 elastoplastic material model in PAM-CRASH, and the plastic response of the nose structural parts was described via the Johnson–Cook (JC) constitutive model which can reflect the hardening effect caused by strain, the strain-rate strengthening effect, and the softening effect of metal materials caused by temperature [24]:

$$\sigma_e = \left[ A + (B) (\varepsilon_e^p)^n \right] \left[ 1 + C \ln \frac{\dot{\varepsilon}}{\dot{\varepsilon}_0} \right] \left[ 1 - \left( \frac{T - T_r}{T_{melt} - T_r} \right)^m \right] \quad (1)$$

where  $\sigma_e$  is the equivalent stress,  $\varepsilon_e^p$  is the equivalent plastic strain,  $\dot{\varepsilon}/\dot{\varepsilon}_0$  is the equivalent strain rate,  $T_{melt}$  is the melting point of the material,  $T$  is the current test temperature,  $T_r$  is the room temperature. A, B, C, n, and m are constant parameters. The equivalent stress,  $\sigma_e$ , and the equivalent strain rate,  $\dot{\varepsilon}/\dot{\varepsilon}_0$ , are intermediate variables in the simulation process.

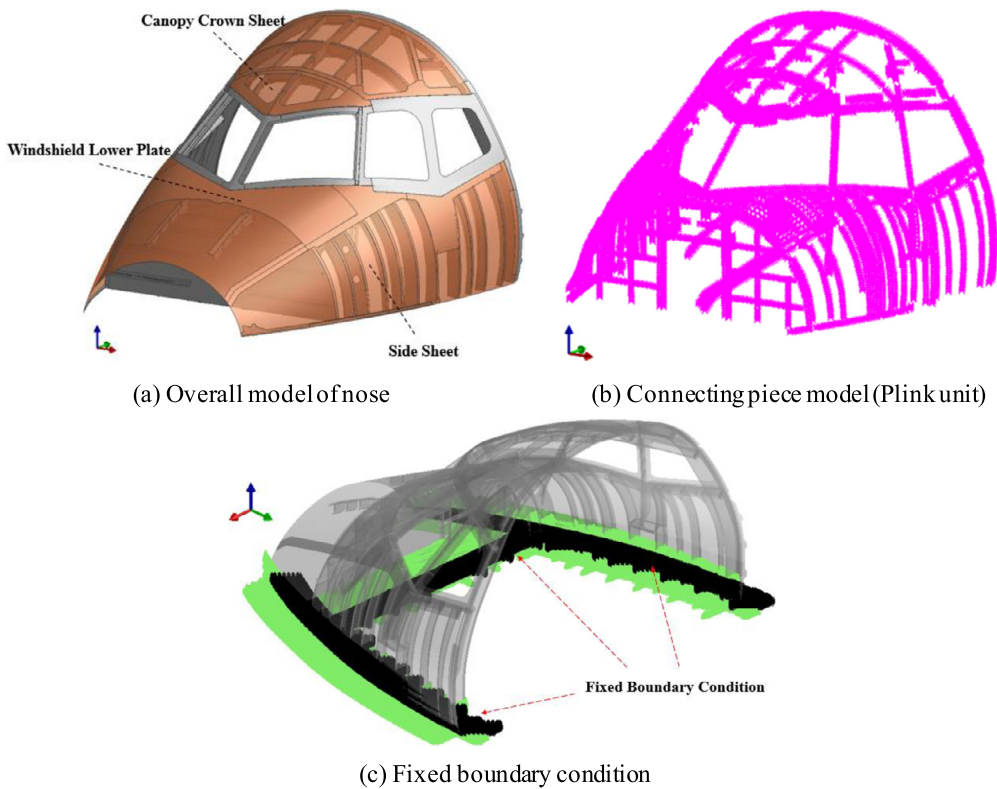


Fig. 1. FE model of the nose.

**Table 1**  
Johnson–Cook constitutive model parameters.

Type of aluminum alloy	A/MPa	B/MPa	C	n	$\varepsilon_{fail}$
2524	315	770	0.0028	0.75	0.15
2024	289.05	410.65	0.04025	0.4935	0.20
7075	473	210	0.033	0.3813	0.14
7050	490.8	530	0.005138	0.5804	0.12
6061	324	114	0.002	0.42	0.12

The material of the canopy crown sheet and the side sheet showed in Fig. 1(a) is the 2524 aluminum alloy and the lower plate of the windshield is made of 2024 aluminum alloy. The edge strips and sheet-metal components are made of the 7075 and 7050 aluminum alloys, respectively. According to transient dynamics, the 2024 and 7075 aluminum alloys are between the intermediate-strain and high-strain rates, all of which presented an apparent strengthening effect on the strain rate [25]. Meanwhile, the hardening effect of the metallic materials caused by strain should also be taken into consideration, whereas the temperature softening effect should be ignored. The failure behavior of the material was determined by the equivalent plastic strain of failure,  $\varepsilon_{fail}$ . In other words, when the equivalent plastic strain of the material reaches  $\varepsilon_{fail}$ , material failure will be confirmed and its cell will be deleted from the FE model. The JC constitutive model parameters of the aforementioned metallic materials have been measured and can be found in the literature [26–29], and their values are listed in detail in Table 1.

The failure criterion of the Plink units is as follows [30]:

$$\left(\frac{N}{T_{max}}\right)^m + \left(\frac{T}{S_{max}}\right)^n = 1 \quad (2)$$

where  $N$  and  $T$  are the tension and shear force, respectively.  $T_{max}$  and  $S_{max}$  are the maximum tension and the maximum shear force, respectively. The maximum tension and maximum shear force of

**Table 2**  
PC material parameters.

Material	Density (kg·mm <sup>-3</sup> )	Young's modulus (GPa)	Poisson's ratio	Yield stress (GPa)
PC	1.18E-6	2.35	0.3	0.062

all Plink units in this study were set to 5.1 kN and 3.2 kN, respectively, and the constant indices  $m$  and  $n$  were set to 1.5 and 2.1, respectively.

## 2.2. FE model of the UAV

The Phantom4 UAV made by DJI is the most popular, light consumer-level UAV in the present market and it has been used in simulation experiments in other countries as well. Through the surveying and mapping of the UAV sponsored by DJI, the mathematical model of the UAV was established in CATIA. The geometry cleanup and grid partition were completed in HyperMesh. Finally, the model pre-treatment was completed after importing the model to PAM-CRASH. The UAV calculation models including configuration, the material distribution and major components are depicted in Fig. 2. The motor, battery, circuit board, camera and pan-tilt were all processed as homogeneous objects and were discretized by the solid unit, whereas the shell unit discretized the enclosure and the paddle. Furthermore, the total number of the solid units and shell units in the UAV model were 5,044 and 8,900, respectively. The camera, pan-tilt and the motor are made of the 6061-T6 aluminum alloy and their mechanical properties are consistent with those of the nose structure listed in Table 1. The material parameters of the PC, the circuit board which is made of glass-epoxy composites, and the battery that is made of Li-Po are listed in Tables 2 [31], 3 [32], and 4 [33,34], respectively. After measurements, the masses of the motor, battery, circuit board, and camera

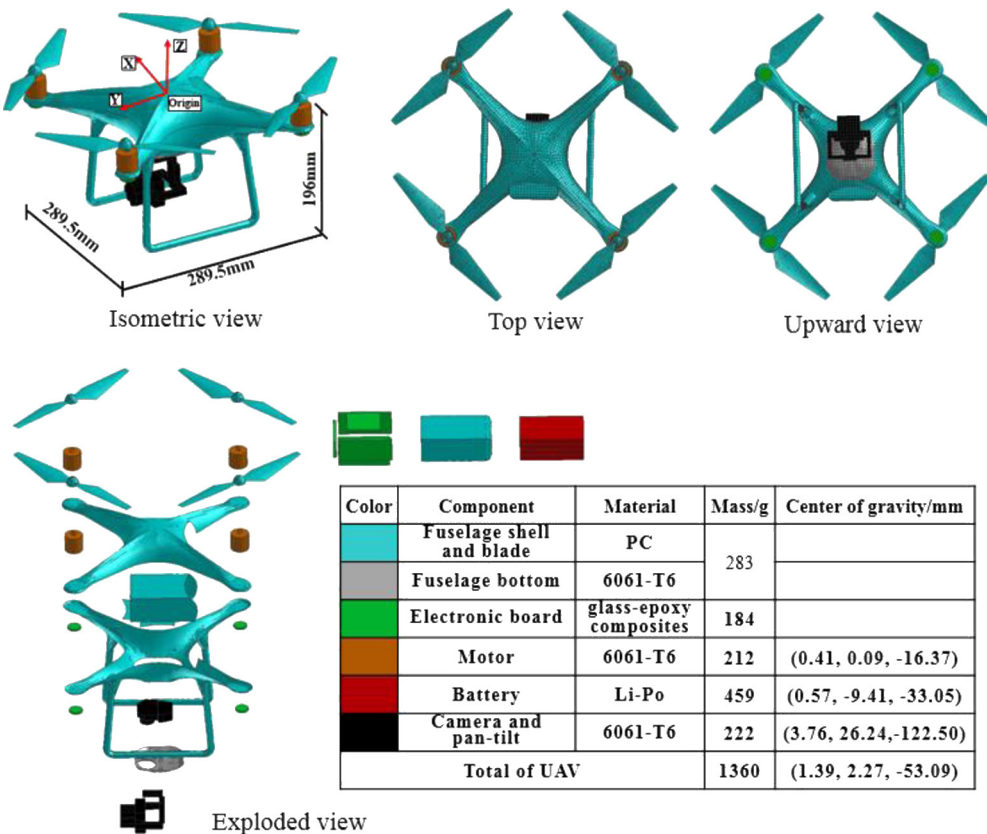


**Fig. 2.** FE model of the UAV. (For interpretation of the colors in the figure(s), the reader is referred to the web version of this article.)

**Table 3**  
Circuit board material parameters.

Density (kg·mm <sup>-3</sup> )	Young's modulus (GPa)		Compressive strength (GPa)		Tensile strength (GPa)		Shear modulus (GPa)	Shear strength (GPa)	Poisson's ratio	
	X	Y	X	Y	X	Y				
1.85E-6	18.83	19.26	0.365	0.3	0.233	0.31	8.275	0.152	0.136	0.118

**Table 4**  
Battery parameters.

Density (kg·mm <sup>-3</sup> )	Young's modulus (GPa)	Poisson's ratio
1.75E-6	0.5	0.01

and pan-tilt of the UAV were 212 g, 459 g, 184 g, and 222 g, respectively, and the total mass of the remaining parts was 283 g.

### 2.3. FE model of bird

Since birds have excellent fluidity in high-speed motion, the relatively mature Smoothed-particle hydrodynamics (SPH) method is typically applied in the modeling of the bird calculation model [18–20]. In this study, the geometrical model of the bird is a cylinder with calottes at both ends and the total length along the longitudinal axis was twice the diameter of section D. The value of D was 0.114 m in the model illustrated in Fig. 3.

Considering the rheological process during the deformation caused by the bird strike, the Murnaghan state equation was used in the bird strike material model [35].

$$P = P_0 + b \left[ \left( \frac{\rho}{\rho_0} \right)^\gamma - 1 \right] \quad (3)$$

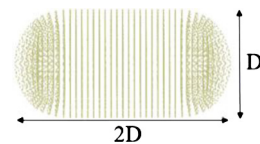


**Fig. 3.** SPH bird calculation model.

where  $P_0$  is the initial reference pressure,  $P$  is the current pressure,  $\rho/\rho_0$  is the ratio of the current density to its initial density,  $b$  is the bulk modulus of elasticity, and  $\gamma$  is the index. According to the literature [30],  $b$ ,  $\gamma$ , and  $\rho_0$  are 2.8 GPa and 7.99 and 936 kg/m<sup>3</sup>, respectively.

### 2.4. Convergence of models

Five mesh sizes are considered, which are 4 mm, 7 mm, 14 mm, 21 mm and 28 mm respectively. Fig. 4 shows an example of an UAV striking the lower panel of the main windshield. Intuitively, the shape of the deformation area of the upper five contour plots shows evident convergence to specific patterns when progressively increasing the mesh density. Two features such as depth of dent and max length of the dent in deformation area are further quantitatively analyzed and compared at different mesh sizes. It can be

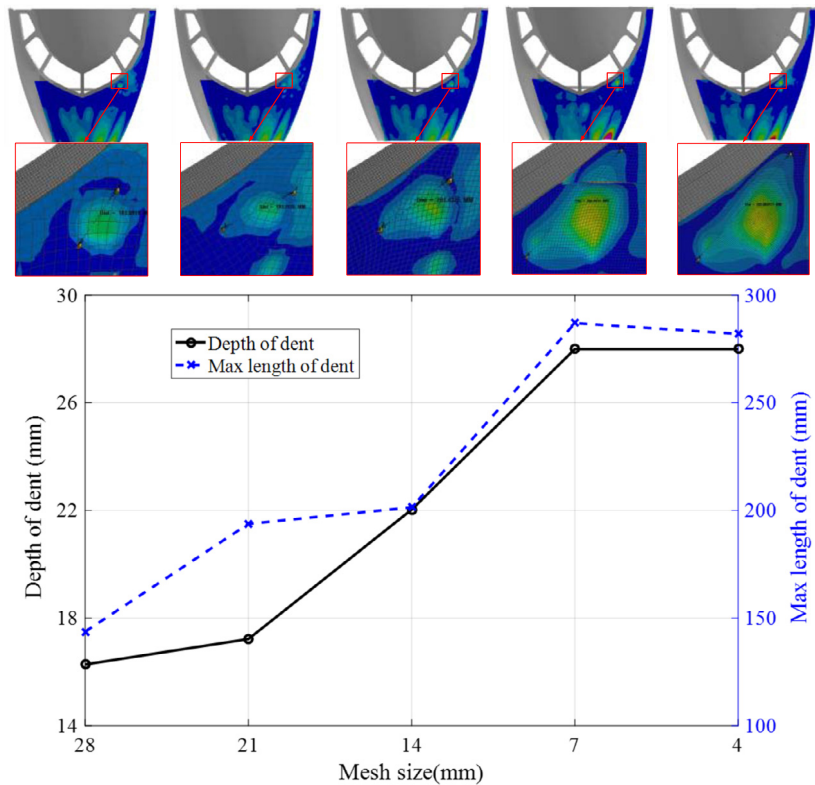


Fig. 4. Mesh convergence of aircraft nose model.

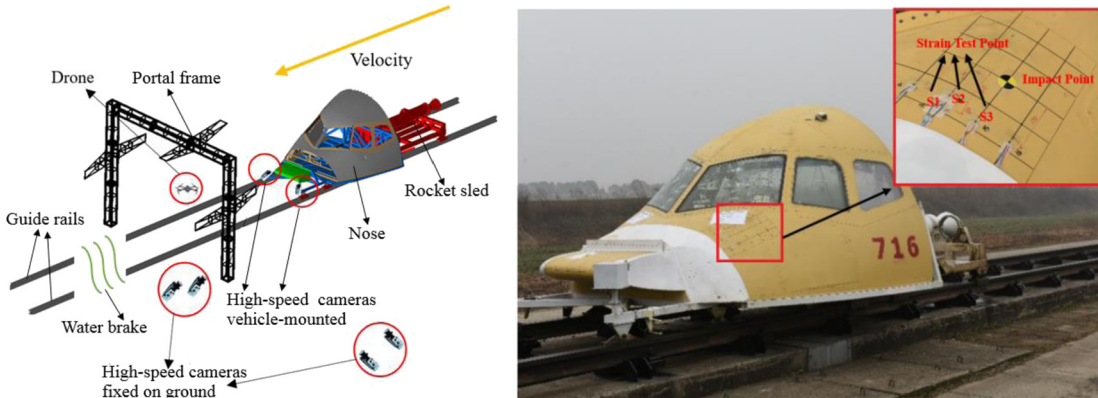


Fig. 5. Test equipment layout.

calculated that the maximum displacement converges to 28 mm and the size of dent damage converges to 280 mm.

### 3. Model validation

#### 3.1. Validation test description

The entire test equipment consisted of the UAV, portal frame, the high-speed cameras and rocket sled which was also composed of a rocket booster, two tracks, a water brake and test articles of the nose. The left picture of Fig. 5 illustrates the test validation equipment layout. The vehicle-mounted cameras with a resolution 200,000 pixels have a photo-frequency 3,000 fps and the cameras fixed on ground with a resolution of 800,000 pixels have a photo-frequency 5,000 fps. The strain testing system with 16 channels has a sampling rate of 50,000 fps and achieves an accuracy of 4%. The UAV was fixed under the portal frame with Kevlar rope, and the booster powered the movement of the test nose toward the

UAV. The speed when the UAV striking the nose could be controlled by calculating the distance between the starting point of the nose and the UAV and the explosive loading quantity of the booster during the movement process. Different from air-cannon tests, the test presented in this study has the feature that the collision can be entirely and realistically simulated with whole-level UAV and full-size aircraft nose and that the UAV is still under its normal operating conditions with rotating blades at the moment of collision. The impact point in the test in the lower plate of the windshield was surrounded by a few grids with a unit length of 100 mm, near which five strain gauges were arranged along the surrounding girds in order to paste accurately. It was a pity that two of gauges were invalid because of violent shock, and the remaining three (S1, S2, and S3) are marked on the right picture of Fig. 5.

A local coordinate system is established by taking intersection of the front-end cross-section of nose (excluding radome), horizontal reference plane, and longitudinal symmetrical section as an

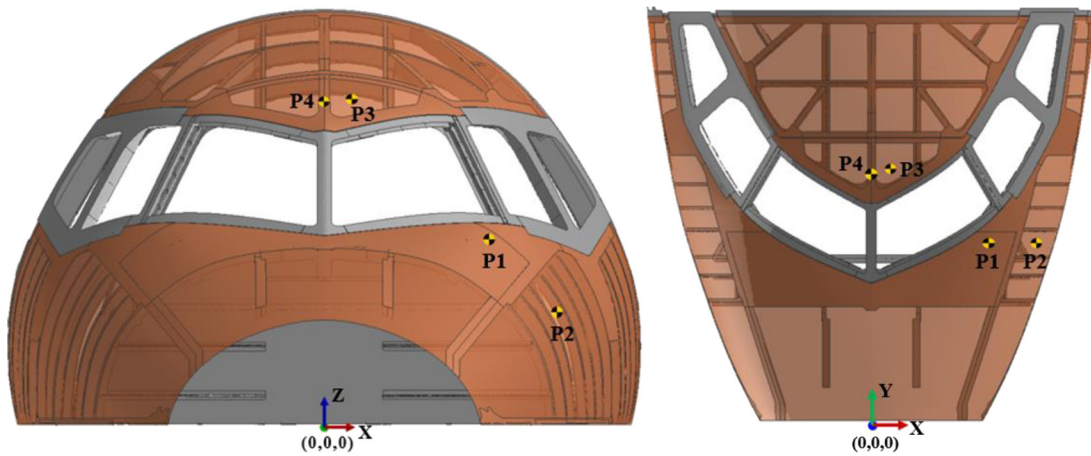


**Fig. 6.** Coordinates of impact points.

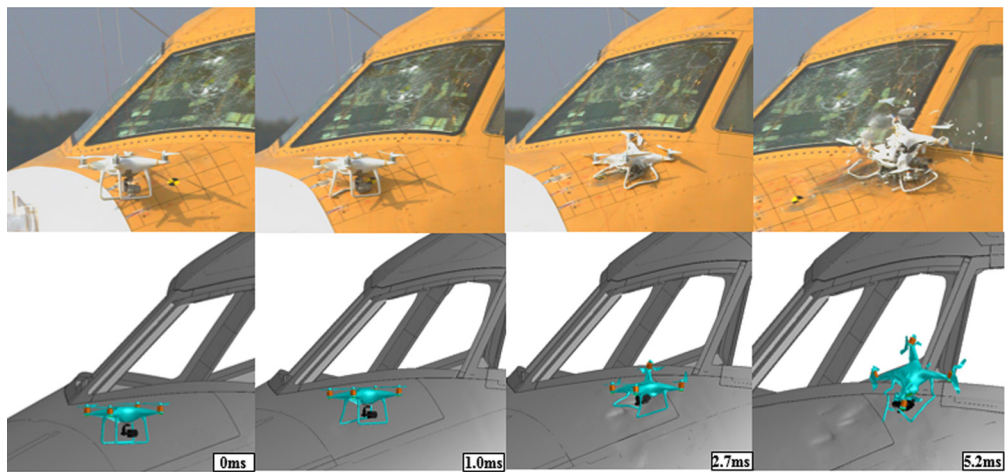


**Fig. 7.** Deformation-process comparison between the impact test and the simulation.

origin, wherein OX axis is positive to left of the course in the horizontal plane, OY axis is positive to inverse heading in the longitudinal symmetry plane of the fuselage, and the orientation of OZ axis is determined in terms of the right-hand rule. Based on this regulation, the coordinate of validation test location in Fig. 5 is (824.0 mm, 1247.5 mm, 938.2 mm) which is labeled as P1 in Fig. 6. The other coordinates of three impact points in the subsequent simulation shown as P2, P3, and P4 in Fig. 6 are (1165.2 mm, 1246.8 mm, 567.6 mm), (135.7 mm, 1778.3 mm, 1638.5 mm), and (0 mm, 1729.8 mm, 1631.5 mm) respectively.

CCAR 91.117, as well as FAR 91.117, states that *unless otherwise authorized by the Administrator, no person may operate an aircraft below 10,000 feet Mean Sea Level (MSL) at an indicated airspeed of more than 250 knots* [36]. At this altitude, the corresponding velocity value converted from the performance parameter of the type of aircraft by engineers is the ultimate impact velocity value of approximately 131 m/s. Meanwhile, considering the average velocity of the UAV of about 20 m/s, the test velocity was predetermined at 151 m/s. The actual impact velocity measured during the test was 152.8 m/s and the error between the actual impact velocity and the predetermined velocity was less than 1%.

### 3.2. Comparison of impact test and simulation

Considering the extremely high financial and time costs, only one collision test between the UAV and the nose of the aircraft was conducted to verify the FE models in the collision test of the

whole-level UVA with the full-size nose. The specific impact location is depicted in Fig. 5.

The comparison of the results at typical moments in the high-speed photography of the collision test and the simulation animation are shown in Fig. 7. As may be seen, the undercarriage of the UAV first comes into contact with the nose, thus causing nose deformation. However, plastic deformation of the nose skin is not generated. Then, the camera strikes the nose skin, clinging to which to slide forward, and deviates from the skin surface after colliding with the rib finally. Therefore, the skin and the internal backing plate are subjected to plastic deformation and have been led into a long and narrow area with pit damage. Subsequently, the fuselage of the UAV containing the circuit board and the battery touches the nose structure and continues moving forward, thus causing the plastic deformation of the skin and of the internal backing plate again. It finally forms an additional long and narrow area with pit damage. The simulation animation is more consistent with the deformation response of the UAV impact test.

The sampling frequency of the strain gauge in the test was 50,000 Hz and the simulation output step size was 0.02 ms. Fig. 8 illustrates the result of the comparison of the strain history between the impact test and the simulation. Compared with the curve obtained from the impact test, differences may be observed in the simulation strain curve because specific parameters could not be accurately set, such as the contact friction coefficient, the connection strength of the UAV components, and the stiffness of

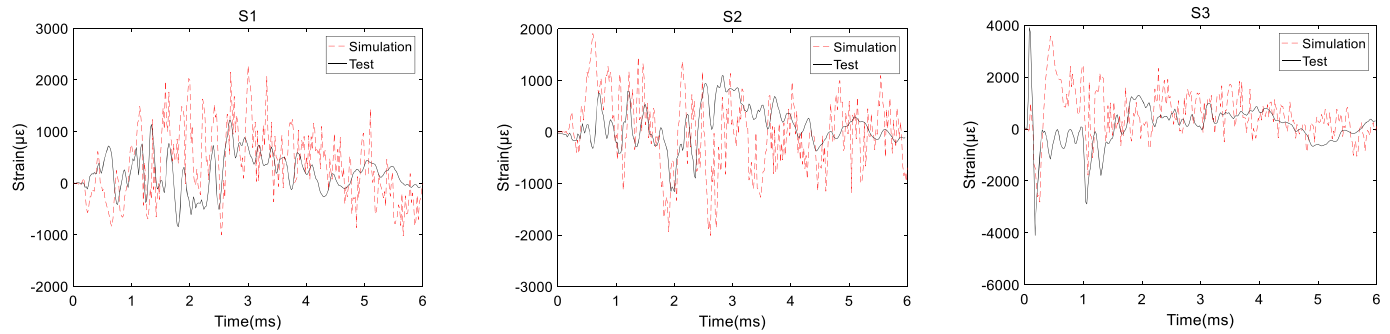


**Fig. 8.** Strain-history comparison between the impact test and the simulation.

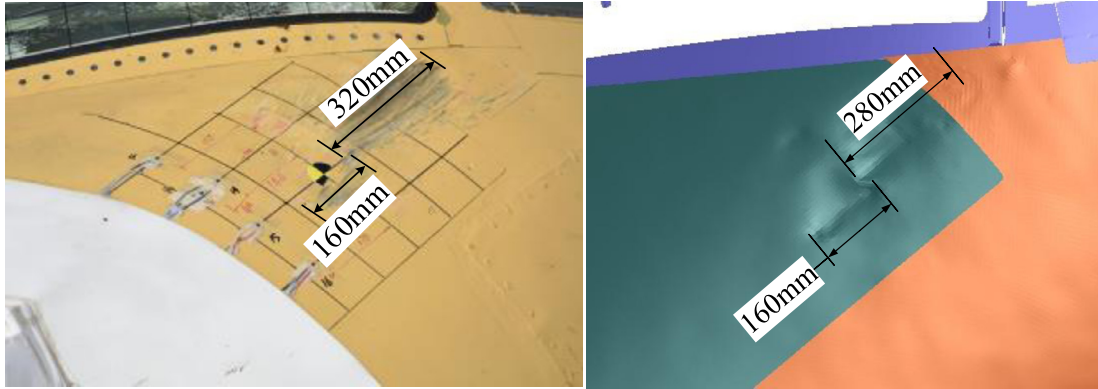


**Fig. 9.** Comparison of the damage size (exterior).



**Fig. 10.** Comparison of the damage size (interior).

the contact between the UAV and the nose. Meanwhile, due to numerous rivets between the strain measuring point and the impact point and the actual rivet distribution not being simulated accurately, the stress wave transmission during the impact process was disturbed and a disturbance could not be remedied in the simulation. Considering the aforementioned influencing factors, the simulation well predicted the strain-response curve trend to a certain extent. It roughly forecasted the peak of the strain-response curve as illustrated in Fig. 8.

The comparison of the external damage between the impact test and the simulation is presented in Fig. 9. The pit damage on the surface can be observed both in the impact test and the simulation, and the scratch may be seen in the impact test as well. By measuring the pit in the simulation, it was found that the simula-

tion results are close to that in the impact test, and the maximum diameter of pits is basically consistent. The internal damage is shown in Fig. 10. In the test, only deformation damage exists in the internal rib strip and the backing plate of the impacted area. However, a small unit deletion (depicted as a 42 mm length crack) may be observed in the internal rib strip and the deformation damage is only seen in the backing plate in the simulation. Based on Fig. 9 and Fig. 10, it could be concluded that the damages existing in the simulation and the test results are rather similar.

From the dynamic deformation of the UAV, the strain response, and the damage results of the nose structure, it can be summarized that the FE simulation models have a certain validity and can be used for the simulation analysis of a UAV that will collide with other parts of the nose structure.

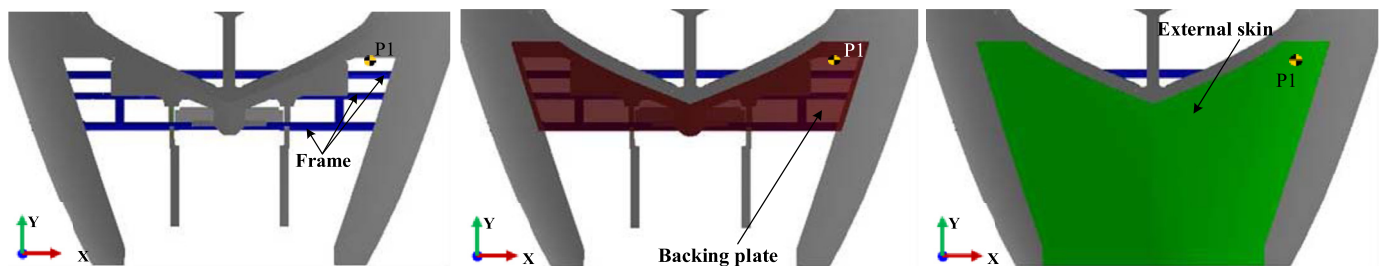


**Fig. 11.** Multi-layer structure diagram of the lower plate.

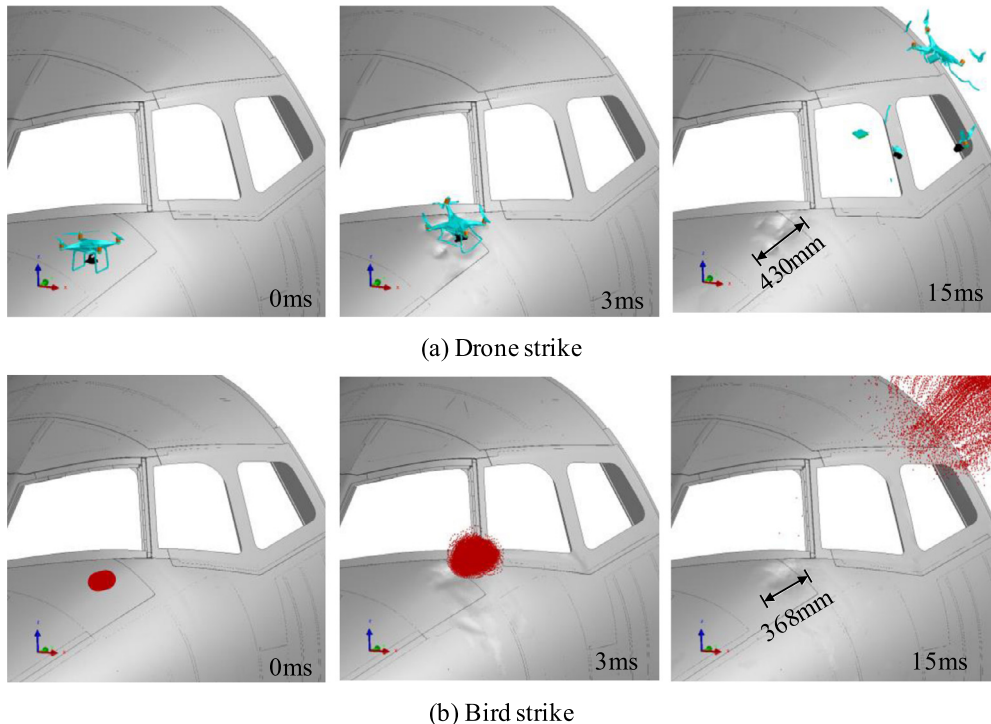


**Fig. 12.** Process and consequence comparison of (a) the UAV and (b) the bird strike on the lower plate of the main windshield.

#### 4. Comparison of the UAV and bird strike simulation

Based on the aforementioned validated model, the anti-UAV impact performance of the lower plate of the main windshield, the side sheet of nose, the crown sheet of the canopy, and the beam of the canopy was studied. In order to explore the applicability of the anti-bird strike airworthiness clauses of the aircraft structure to the anti-UAV strike of the aforementioned four typical structures, the requirement of airworthiness against bird-striking was implemented as a condition in the simulation input. The dynamic response and the damage result were analyzed when the UAV and the bird had struck the structures. The projection of the center of gravity of the UAV and the bird on the nose structure along the reverse direction of the aircraft course was considered as the impact targets. Furthermore, the initial velocities of both the 1,800 g bird and 1,360 g UAV were set to 152 m/s.

##### 4.1. Lower plate of main windshield

The impact point at the lower plate of the main windshield was consistent with that in the previous section 3.1 and the coordinate of that is (824.0 mm, 1247.5 mm, 938.2 mm). In addition to the skin on the surface, there was a backing plate inside as shown in Fig. 11, which contributed to the reinforcement of the

impact-resistance ability. The typical processes and consequences of a collision between a UAV or bird and the lower plate are shown in Fig. 12. Both the UAV and the bird “skim” through the nose structure and create pit damage, however, neither caused any penetration injury. Actually, as can be seen from Fig. 10 that there is tiny internal damage. Therefore, it may be concluded that the lower plate of the windshield can resist an impact of a 1,360 g UAV or a 1,800 g bird.

##### 4.2. Side sheet of nose

In this section, the single skin region between two edge strips located at the side sheet is considered as the collision area which is a weak zone for the side sheet because it only has a stressed-skin construction. The coordinate of impact location corresponding to P2 in Fig. 6 is (1165.2 mm, 1246.8 mm, 567.6 mm) and the processes and consequences of the UAV and bird collision on the side sheet are illustrated in Fig. 13. The bird has only caused the failure of several rivets and a few pits in the external skin, however, the battery of the UAV has caused a large crack in the skin that would further propagate. Furthermore, the UAV-striking exacerbates the destruction of three edge strips inside the nose displayed in Fig. 14.

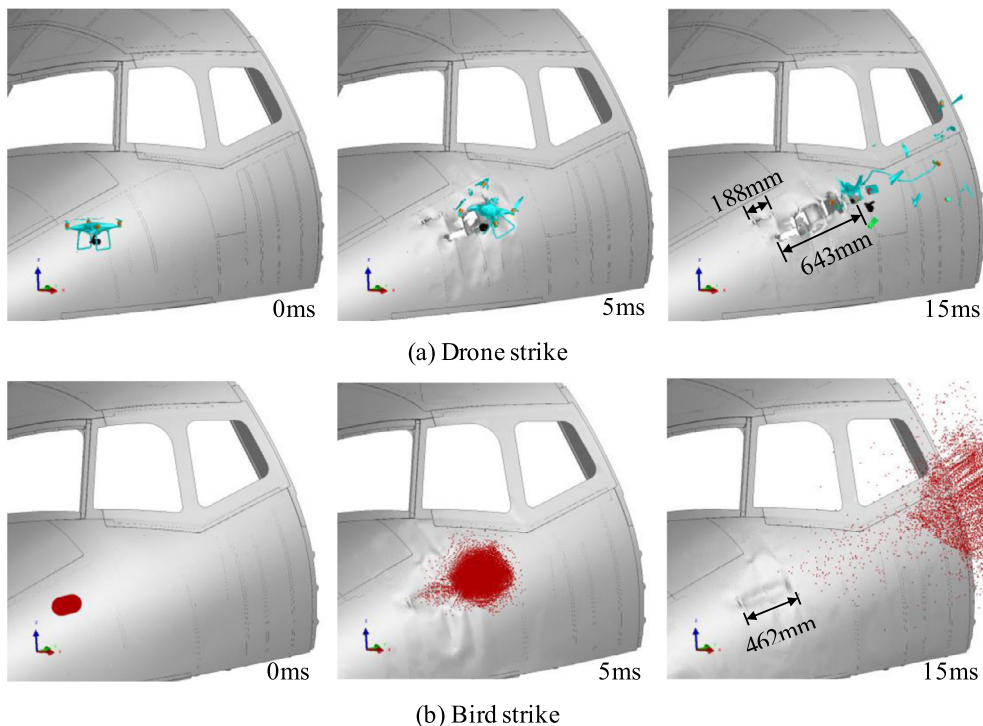


**Fig. 13.** Process and consequence comparison of (a) the UAV and (b) the bird strike on the side sheet.

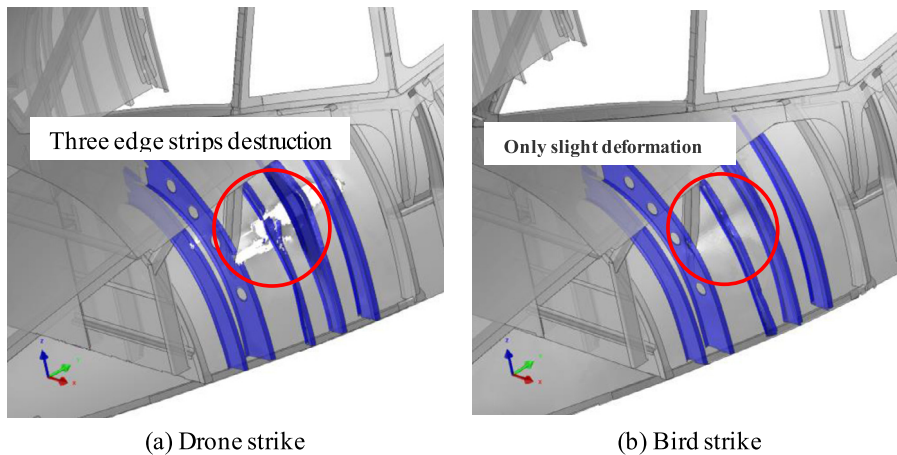


**Fig. 14.** Comparison of internal damage of the side sheet by (a) UAV and (b) bird strike.

Obviously, the damage caused by drone strike on the side sheet of the nose is much more serious than that caused by bird strike. Therefore, the side sheet can resist the strike of a 1,800 g bird but cannot resist the collision of a 1,360 g UAV at 152 m/s.

#### 4.3. Crown sheet of canopy

In this section, the left crown sheet of the canopy is taken as the collision area which is a weak zone with a single skin of impact resistance. The coordinate of impact location corresponding to P3 in Fig. 6 is (135.7 mm, 1778.3 mm, 1638.5 mm) and the collision processes and the consequences of a UAV and a bird collision on the crown sheet of the canopy are shown in Fig. 15. The bird “skims” over the nose and causes deformation pit damage only. By contraries, the motor, camera, and battery of the UAV tear the skin successively and the damage size is much larger than that caused by bird strike. As seen from the internal scene of the

nose in Fig. 16, the battery is trapped in the nose structure, which maybe leads to a hidden danger of explosion, and there is serious damage to beam fracture by UAV strike. Therefore, the crown sheet of the canopy can resist a collision of a 1,800 g bird, whereas cannot resist the collision of the 1,360 g UAV at 152 m/s.

#### 4.4. Beam of canopy

Longitudinal beams are the main load-bearing component of crown sheet of the canopy and they are another typical parts supporting the external single skin of the nose for resisting UAV strike. The coordinate of impact location corresponding to P4 in Fig. 6 is (0 mm, 1729.8 mm, 1631.5 mm) and the collision processes and the consequences of a UAV and a bird collision on the beam of the canopy are shown in Fig. 17. The bird “skims” over the skin supported by a longitudinal beam and leaves litter scratch. While the camera, motor, and battery of the UAV collide with the nose one

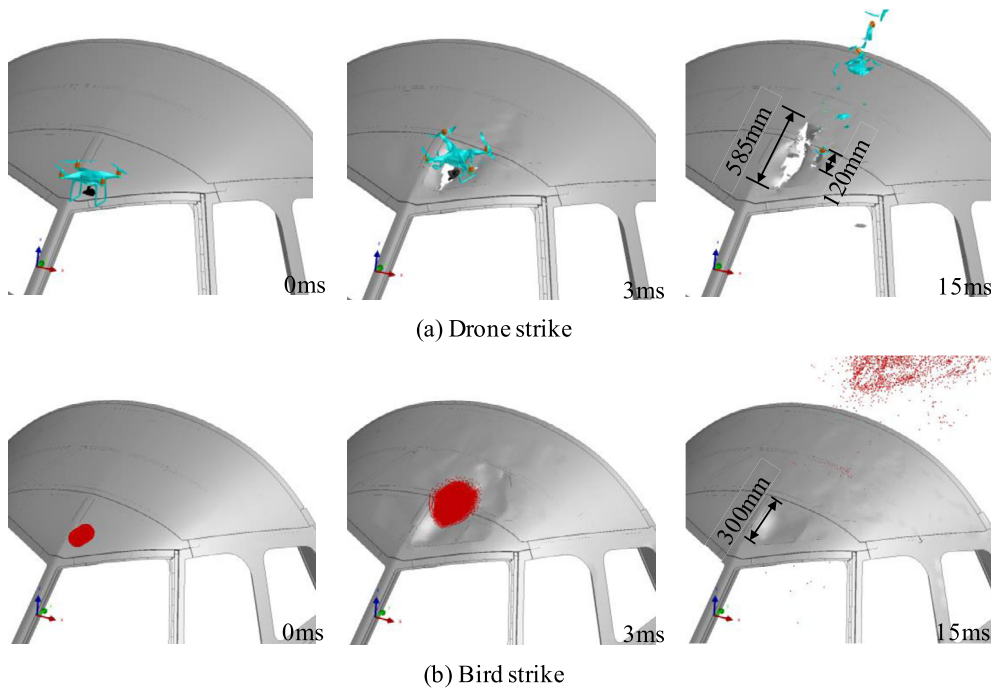


**Fig. 15.** Process and consequence comparison of (a) the UAV and (b) the bird strike on the crown sheet of the canopy.

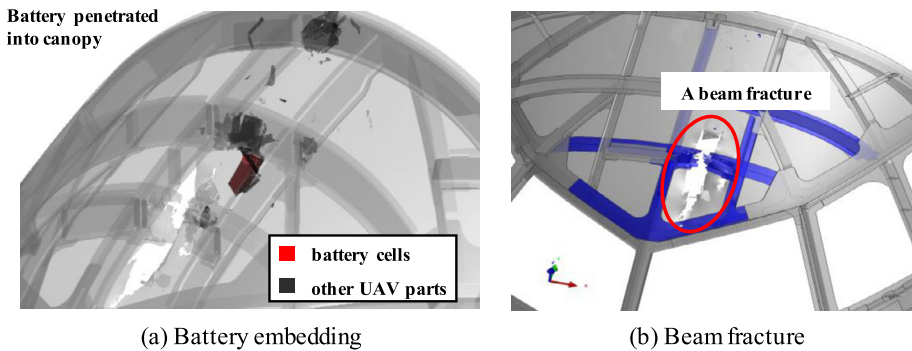


**Fig. 16.** (a) Internal hidden danger and (b) damage of crown sheet of canopy by UAV strike.

after another and adhere to the skin throughout the course of the UAV strike. The beam is not affected by the impact of these rigid components, however, the skin across both sides of the main beam is slightly punctured by two motors at the front end of UAV. Therefore, the main beam of the canopy can resist an impact of a 1,360 g UAV or a 1,800 g bird, and yet the skin around the beam would be broken slightly by the motors of the UAV.

## 5. Analysis of dynamic response

There are process and consequence comparisons of the UAV and the bird strike at four typical locations in Section 4 and the simulation responses are analyzed in this section. Strain responses of the nose after UAV and bird strike at steady-state moment are indicated in Fig. 18, seen from which that the maximum principal strain of nose by UAV strike is closer to that by bird strike at P1 position with no surface penetration and internal damage. However, the maximum principal strains of nose by UAV strike are much larger than that by bird strike at P2, P3, and P4 positions with skin penetration and internal damage under the first two conditions of these three points. It is obvious that load-bearing beam takes an effect on damage mitigation and reducing maximum principal strain of nose by UAV or bird strike for P3 and P4.

From the view of contact force exhibited in Fig. 19, the greater the amplitude of contact force does not mean that the damage is more serious. The contact force amplitude of UAS collision is twice as high as that of bird strike at P1 position and is almost equal to that of bird strike at P1, P2, and P3 position. However, the impact consequences at P2 and P3 are much more severe than that at P1 and P4. It may be explained as follows. On the one hand, the bird material displayed fluid mechanics characteristics during the impact process with high speed and would splash as shown in the Fig. 12(b), Fig. 13(b), Fig. 15(b), and Fig. 17(b), which would increase contact area and mitigate impact loading. Whereas the UAV displayed rigid mechanics characteristics because of the hardened existence such as motor, battery, and camera which occupy most mass of the UAV. Therefore the impact loading was more concentrated and easier to cause local surface penetration and internal damage. On the other hand, the bird body was approximately assumed to be a homogeneous entity in the simulation according to conventional practice shown in references [18–22]. However, the UAV was made of various components with different densities most of which are much higher than that of bird. These hard components have displayed discreteness during the course of collision and caused local high-stress areas in instantaneous which is demonstrated with quite narrow amplitude pulse width rather

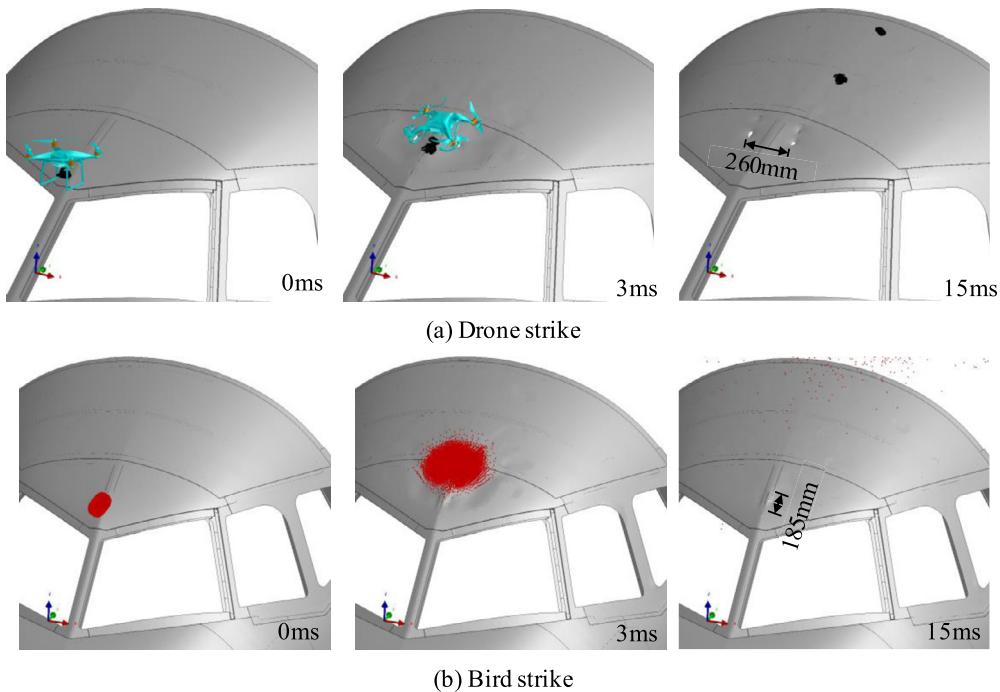


**Fig. 17.** Process and consequence comparison of (a) the UAV and (b) the bird strike on the beam of the canopy.

than that of bird strike in Fig. 19. As a result, these hard blocks caused local perforation of the external skin and even damage to internal parts.

The simulation responses of energy at four impact positions are exhibited in Fig. 20. The initial kinetic energy of bird is 33% greater than that of UAV, and the kinetic energy loss of bird and UAV during the course of collision is converted into internal energy of nose, the internal energy of UAV, and other energy. The kinetic energy loss of bird is less than that of UAV and the absorbed internal energy of nose by UAV strike is greater than that by bird strike at each impact point. It maybe also explains why the damage of the nose was more serious by UAV strike with the same collision conditions of UAV and bird. It can also be seen from Fig. 20 that the response time for the kinetic energy of UAV towards a steady state after collision is longer than that of bird, which indicates that the damage of nose would not deteriorate further after instantaneous impact by bird, whereas sustained deformation and penetration happened to nose skin during the impact of UAV and nose. The mentioned scenario above is consistent with the sense observed in simulation animation and test process. In the energy distribution by UAV strike, the residual kinetic energy of UAV at impact position P2 and P3 is much less than that at impact position P1 and P4, however nose internal energy at impact position P2 and P3 is much more than that at impact position P1 and P4, which is the evidence that the greater the kinetic energy loss, the more serious the damage of nose was. The kinetic energy of UAV and bird didn't fall close to zero due to the characteristic of "easily slip away along upper slope or side of nose" during the collision, which is different from orthogonal collision between UAV and the tail leading edge in reference [9].

## 6. Influence of UAV flight posture

According to the simulation results of collision at four typical positions in Section 4, the skin and/or reinforcements of the nose were both broken by UAV strike at P2, P3 and P4 with normal posture, which means that it would be no longer necessary to study the impact postures of UAV at these positions. There was no pene-

trating damage to the skin at P1 with norm posture of UAV, however it is unknown whether the lower panel would be penetrated by UAV strike with other possible postures. Based on the performance parameters of this type of UAV, the angle ranges of pitching around X axis, yawing around Y axis and rolling around Z axis are set to  $(-45^\circ, 45^\circ)$  in the local coordinate system with the center of gravity of UAV as an origin as displayed in Fig. 21. With the application of space-filling Latin hypercube based sampling method [37], a total of 35 impact postures of UAV are designed, not including the posture at P1 in Section 4.1, as shown in Table 5. The skin of the nose was deformed differently, however no penetration has happened in all the above scenes. The kinetic energy loss of UAV and peak of contact force of collision are exhibited in Fig. 22 with 36 impact postures of UAV, including deformation results of nose corresponding to maximum and minimum kinetic energy loss of UAV respectively.

The research findings in this section make clear that it is safe for the lower panel of the nose to collide with the 1360 g UAV when the aircraft is flying at an altitude not higher than 10,000 feet.

## 7. Summary and expectation

In this present study, the collision safety of the specific locations of the aircraft nose with the whole-level UAV was investigated by conducting both simulations and a full-scale test in the case of complying with the regulation of CCAR 25.571 (same to FAR 25.571) and CCAR 91.117 (same to FAR 91.117). From the analysis and discussion above, the preliminary conclusions are summarized as follows.

(1) Owing to the high density, hardness, and concentrated mass of the materials used in the manufacturing of UAV components, a 1,360 g UAV can cause more severe damage to the nose than a 1,800 g bird with the same velocity of 152 m/s, despite the fact that its kinetic energy is only about 75% of that of the bird. Furthermore, the battery of UAV would penetrate the skin to enter the inside of nose at one impact position, which is a huge risk source of causing secondary explosion and fire and is worthy of further deep investigation.

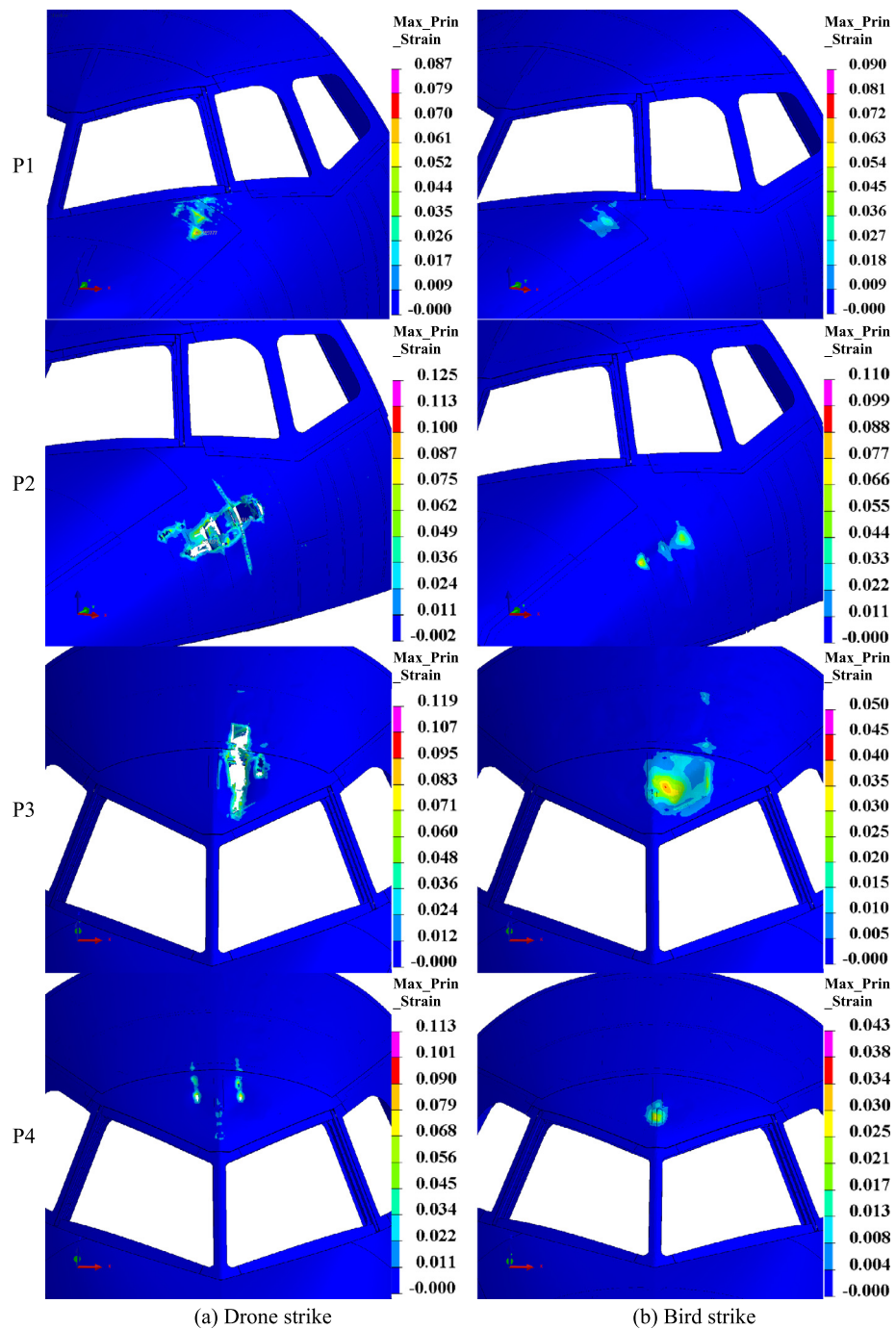


**Fig. 18.** Strain responses of the nose by (a) the UAV and (b) the bird strike.

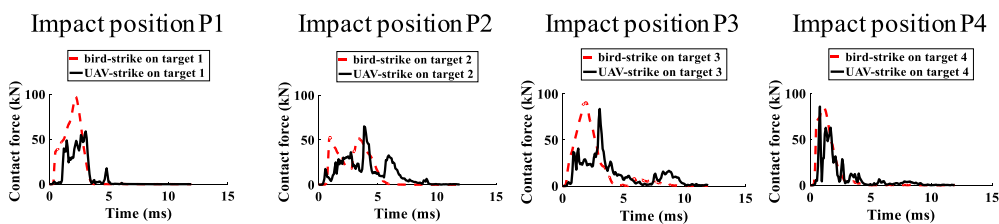


**Fig. 19.** Contact force curves of the UAV and the bird strike.

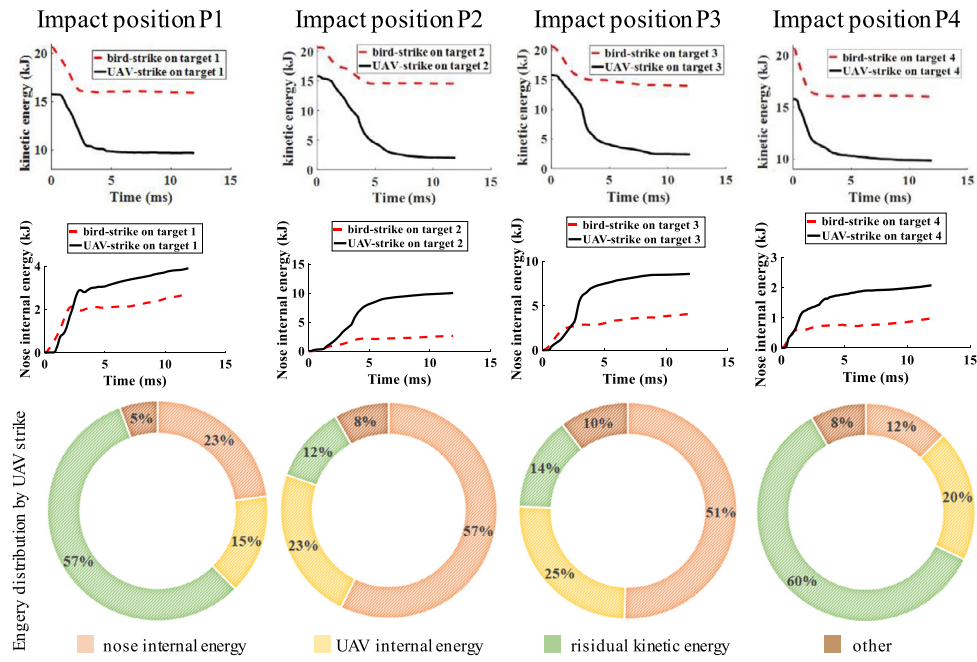


Fig. 20. Energy responses and distributions of four impact positions.

**Table 5**  
Multi-attitudes of UAV strike.

Index	pitch/°	roll/°	yaw/°	Index	pitch/°	roll/°	yaw/°
1	0.63	-2.73	33.43	19	22.59	-39.76	18.01
2	-3.59	26.58	-22.90	20	-3.06	-35.85	16.46
3	26.57	-10.76	0.14	21	44.88	33.96	44.79
4	-21.08	2.52	-6.44	22	-44.75	36.71	-11.51
5	-15.62	29.50	10.45	23	11.53	40.10	25.10
6	28.85	-43.90	-12.90	24	-37.05	-41.53	-39.04
7	-40.91	-32.24	22.77	25	-13.02	-45.00	40.46
8	38.82	44.36	-32.05	26	43.63	4.03	-44.81
9	-35.04	9.70	42.58	27	20.05	19.26	37.34
10	17.51	-25.20	-42.75	28	4.16	12.61	4.43
11	-29.63	9.44	-29.71	29	-17.88	-29.92	-32.98
12	14.11	-8.28	-24.31	30	9.40	-19.12	43.88
13	-36.14	44.53	39.00	31	-24.04	41.57	-44.23
14	-26.86	2.36	31.15	32	-32.20	-16.45	12.64
15	7.50	24.58	-42.28	33	37.28	7.47	20.69
16	-9.96	-12.81	-15.00	34	33.07	-28.89	35.34
17	41.65	-22.93	7.34	35	30.39	15.70	-36.93
18	34.21	27.52	-1.15				

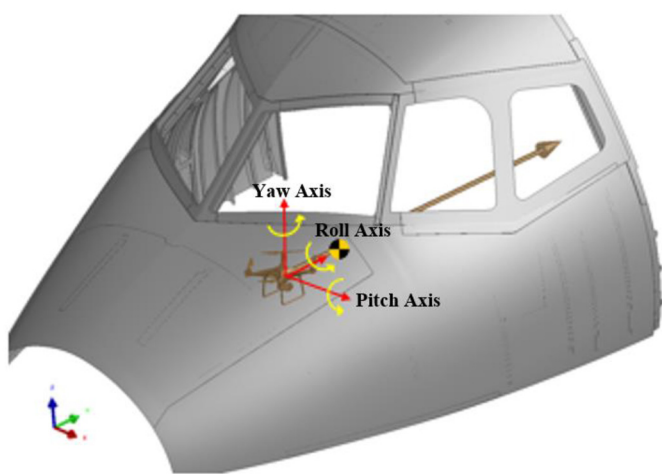
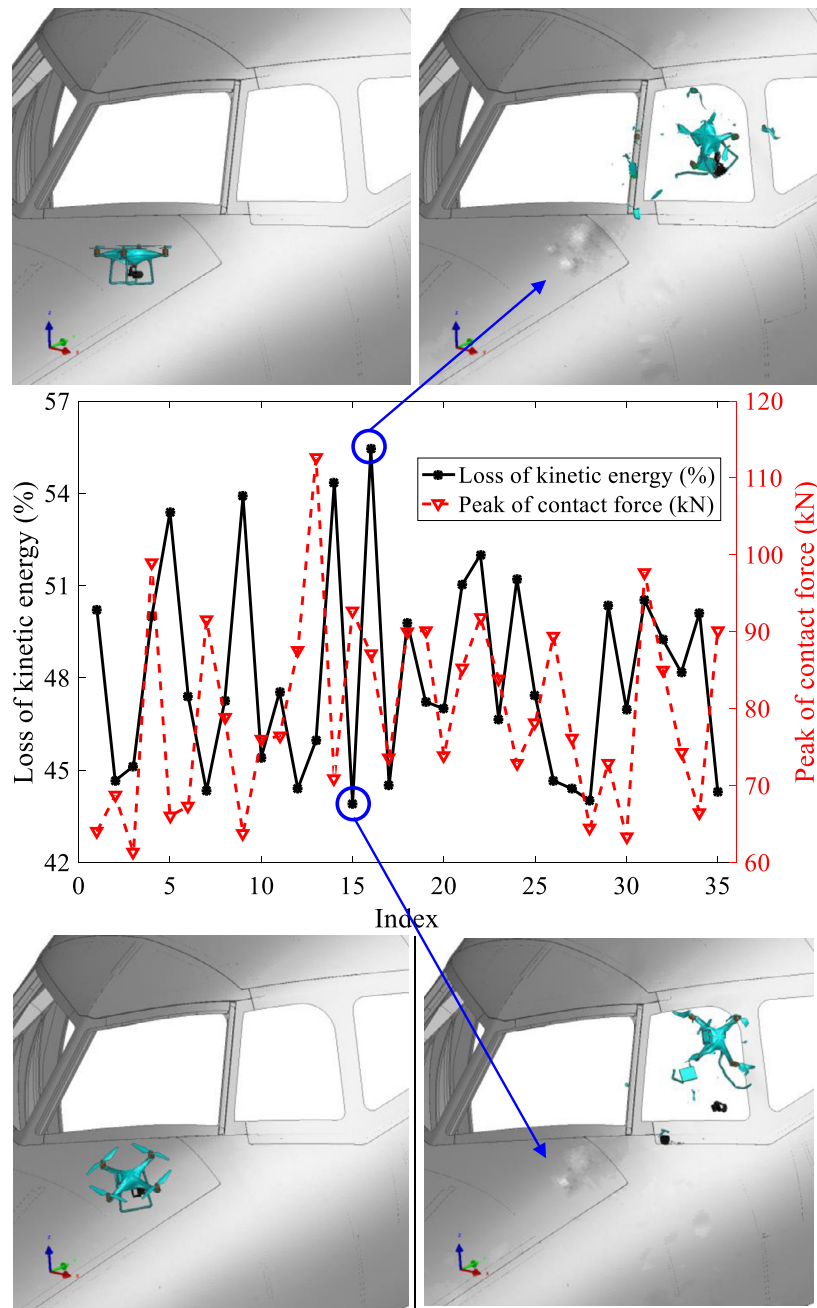


Fig. 21. Schematic diagram of attitude change of UAV.

(2) The contact force amplitudes of collision aren't applicable to evaluate the damage severity of nose which is more reasonable to be explained by the kinetic energy loss of impactors yet. The greater the kinetic energy loss, the more serious the damage of nose is in general and the kinetic energy of UAV as well as the hardness of its major components plays a critical role in evaluating damage of the nose.

(3) The agreement between the simulation results and the test findings in this paper is acceptable, which proves the feasibility and rationality of the numerical simulation method, and can be further used as an efficient approach to investigate the evaluation of collision damage and optimization of the nose in the future.

(4) Currently, the anti-bird strike airworthiness clauses concerning the aircraft nose as CCAR 25.571 are not suitable for the design of the nose against UAV strike. As a result, the operational requirements and supervision policies of UAVs should be improved and extensive studies should be conducted regarding the aircraft design guidelines against UAV strike and the design standards for a UAV collision mitigation additionally such as investigated in reference [38]. According to the simulation results, the damage of nose



**Fig. 22.** Curves of kinetic energy loss of UAV and contact force peaks of collision.

at impact points P1 and P4 was much more mitigative due to backing plates and frames supporting behind than that at impact points P2 and P3, which declares that the reinforced design could resist the UAV collision with high speed.

(5) Different flying postures of UAV would result in various severity damage to nose during the collision. However it is a voluminous project to find the harshest flying postures of UAV and gain the critical breakdown velocities at every collision area and is reserved for future research. The height limit of 400 feet for small UAVs specified in 14 CFR Part 107 of America [1] may be a conservative valuation that would be further validated and is likely to be incorporated into the design guidelines and operational practice of UAV.

(6) Because of the existence of only several types of UAVs with different characteristics, the research results are not sufficient for the improvement of aircraft design or for the amendment of air-

craft operating regulations. It is worth further developing more specialized verification test methods and more universal simulation analysis technologies applicable to various conditions.

#### Declaration of competing interest

No conflict of interest exists in the revised submission of this manuscript, and manuscript is approved by all authors for publication.

#### Acknowledgement

We would like to express our sincere gratitude to the Shanghai Aircraft Design and Research Institute, the Northwestern Polytechnical University, and DJ-Innovations for their valuable help in the modeling of a specific aircraft and the UAV that were employed in

the present work. Moreover, the authors appreciate the Shanghai Aircraft Airworthiness Certification Center for providing a golden opportunity for the present project study.

## References

- [1] FAA, CRF14, Part 107-Small Unmanned Aircraft Systems, FAR 107, 2016.
- [2] FAA, UAS Airborne Collision Severity Evaluation-Structural Evaluation, Final Report Volume I, Springfield, Virginia, 2017, pp. 11–18.
- [3] FAA, UAS Airborne Collision Severity Evaluation-Quadcopter, Final Report Volume II, Springfield, Virginia, 2017, pp. 8–128.
- [4] FAA, UAS Airborne Collision Severity Evaluation-Fixed Wing, Final Report Volume III, Springfield, Virginia, 2017, pp. 8–99.
- [5] FAA, UAS Airborne Collision Severity Evaluation-Engine Ingestion, Final Report Volume IV, Springfield, Virginia, 2017, pp. 18–57.
- [6] R. Alexander, Potential damage assessment of a mid-air collision with a small UAV, Civil Aviation Safety Authority of Australia report, 2013, pp. 9–17.
- [7] British Military Aviation Authority, Small remotely piloted aircraft systems drone midair collision study, Report-16, 2016, pp. 9–16.
- [8] X. Lu, X. Liu, Y. Li, et al., Simulations of airborne collisions between drones and an aircraft windshield, *Aerosp. Sci. Technol.* 98 (2020) 105713.
- [9] X. Meng, Y. Sun, J. Yu, et al., Dynamic response of the horizontal stabilizer during UAS airborne collision, *Int. J. Impact Eng.* 126 (2019) 50–61.
- [10] C. Chen, Y. Guo, J. Liu, et al., Research on dropping test and numerical simulation for unmanned aerial vehicle, *Int. J. Crashworthiness* (1) (2021) 1–17.
- [11] Y. Song, B. Horton, J. Bayandor, Investigation of UAS ingestion into high-bypass engines, part 1: bird vs. drone, in: AIAA/ASCE/AHS/ASC Structures, Structural Dynamics, and Materials Conference, Grapevine, Texas, 2017, pp. 1–9.
- [12] K. Schroeder, Y. Song, B. Horton, et al., Investigation of UAS ingestion into high-bypass engines, part 2: parametric drone study, in: AIAA/ASCE/AHS/ASC Structures, Structural Dynamics, and Materials Conference, Grapevine, Texas, 2017, pp. 1–10.
- [13] H. Liu, M. Man, K.H. Low, UAV airborne collision to manned aircraft engine: damage of fan blades and resultant thrust loss, *Aerosp. Sci. Technol.* 113 (2021) 106645.
- [14] L. Hu, H. Mohd, F.N. Bing, et al., Airborne collision evaluation between drone and aircraft engine: effects of position and posture on damage of fan blades, in: AIAA AVIATION 2020 Forum, 2020.
- [15] H. Liu, M. Man, F.N. Bing, et al., Airborne collision severity study on engine ingestion caused by harmless-categorized drones, in: AIAA Scitech 2021 Forum, 2021.
- [16] T. Lyons, K. D'Souza, Parametric study of a unmanned aerial vehicle ingestion into a business jet size fan assembly model, *J. Eng. Gas Turbines Power* 141 (7) (2019) 071002.
- [17] Y. Wang, The research on design and analysis of civil aircraft opposed to bird-strike, *Chin. Sci. Technol. Inf.* (16) (2014) 40–41.
- [18] L. Qiu, Y. Wang, Analysis and optimize of bird impact dynamic response for civil aircraft's side wainscot structure, *Civ. Aircr. Des. Res.* (2) (2011) 46–51.
- [19] J. Wang, C. Song, J. Liu, The optimizing research on bird-strike resistance of the top nose skin for a large commercial aircraft, *Civ. Aircr. Des. Res.* (1) (2014) 42–45.
- [20] J. Liu, Y. Li, X. Gao, et al., A numerical model for bird strike on sidewall structure of an aircraft nose, *Chin. J. Aeronaut.* 27 (3) (2014) 542–549.
- [21] Y. Zhou, Y. Sun, T. Huang, et al., SPH-FEM simulation of impacted composite laminates with different layups, *Aerosp. Sci. Technol.* 95 (2019) 105469.
- [22] Y. Zhou, Y. Sun, W. Cai, Bird-striking damage of rotating laminates using SPH-CDM method, *Aerosp. Sci. Technol.* 84 (2019) 265–272.
- [23] J. Zhou, J. Liu, X. Zhang, et al., Experimental and numerical investigation of high velocity soft impact loading on aircraft materials, *Aerosp. Sci. Technol.* 90 (2019) 44–58.
- [24] J. Pothnis, Y. Perla, H. Arya, et al., High strain rate tensile behavior of aluminum alloy 7075 T651 and IS 2062 mild steel, *J. Eng. Mater. Technol.* 133 (2) (2011) 21–26.
- [25] C. Xie, M. Tong, F. Liu, et al., Numerical analysis and experimental verification of bird impact on civil aircraft's horizontal tail wing leading edge, *J. Vib. Shock* 34 (14) (2015) 172–178.
- [26] F. Liu, J. Zhang, M. Tong, et al., Dynamic tests and bird impact dynamic response analysis for a 2024-T3 aluminum alloy plate, *J. Vib. Shock* 33 (4) (2014) 113–118.
- [27] C. Xie, M. Tong, F. Liu, et al., Dynamic tests and constitutive model for 7075-T6 aluminum alloy, *J. Vib. Shock* (18) (2014) 110–114.
- [28] J. Tan, M. Zhan, S. Liu, et al., A modified Johnson-Cook model for tensile flow behaviors of 7050-T7451 aluminum alloy at high strain rates, *Mater. Sci. Eng. A* 631 (1) (2015) 214–219.
- [29] A. Long, M. Wan, W. Wang, et al., Forming methodology and mechanism of a novel sheet metal forming technology-electromagnetic superposed forming, *Int. J. Solids Struct.* (2018) 165–180.
- [30] P. Xue, N. Zhao, J. Liu, et al., Approach to assess bird strike resistance for a wing slat structure, *J. Aircr.* 48 (3) (2015) 1095–1098.
- [31] Z. Yin, T. Wang, Investigation of tensile deformation behavior of PC ABS and PC/ABS blends from low to high strain rates, *Appl. Math. Mech.* 33 (4) (2012) 434–443.
- [32] K. Ravi, Mechanical properties of G-10 glass-epoxy composite, *Chandar* (2007) 1–10.
- [33] E. Sahraei, J. Meier, T. Wierzbicki, Characterizing and modeling mechanical properties and onset of short circuit for three types of lithium-ion pouch cells, *J. Power Sources* 247 (2) (2014) 503–516.
- [34] E. Sahraei, R. Hill, T. Wierzbicki, Calibration and finite element simulation of pouch lithium-ion batteries for mechanical integrity, *J. Power Sources* 201 (3) (2012) 307–321.
- [35] M. Amccarthy, J. Rxiao, C. Tmccarthy, et al., Modelling bird impacts on an aircraft wing, part 2: modelling the impact with an SPH bird model, *Int. J. Crashworthiness* 10 (1) (2005) 51–59.
- [36] F.A.A., General Operation and Flight Rules, FAR91.117, 2016.
- [37] V.R. Joseph, E. Gul, S. Ba, Designing computer experiments with multiple types of factors: the MaxPro approach, *J. Qual. Technol.* 52 (4) (2020) 343–354.
- [38] K. Edgerton, G. Throneberry, A. Takeshita, et al., Numerical and experimental comparative performance analysis of emerging spherical-caged drones, *Aerosp. Sci. Technol.* 95 (2019) 105512.